

Article

Numerical Investigations on the Jet Dynamics during Cavitation Bubble Collapsing between Dual Particles

Zhifeng Wang^{1,2}, Zhengyang Feng¹, Jinsen Hu¹ , Yuning Zhang^{1,*} and Yuning Zhang^{3,4}

¹ Key Laboratory of Power Station Energy Transfer Conversion and System (Ministry of Education), School of Energy Power and Mechanical Engineering, North China Electric Power University, Beijing 102206, China; zhifeng.wang@ncepu.edu.cn (Z.W.); zhengyang.feng@ncepu.edu.cn (Z.F.); hujinsen@ncepu.edu.cn (J.H.)

² State Power Investment Corporation, Beijing 100029, China

³ College of Mechanical and Transportation Engineering, China University of Petroleum-Beijing, Beijing 102249, China; zhangyn04@cup.edu.cn

⁴ Beijing Key Laboratory of Process Fluid Filtration and Separation, China University of Petroleum-Beijing, Beijing 102249, China

* Correspondence: y.zhang@ncepu.edu.cn

Abstract: The jet dynamics during cavitation bubble collapsing between unequal-sized dual particles are investigated utilizing a numerical model that combines the finite volume approach alongside the volume of fluid approach. The model incorporates the compressibility of the two-phase fluid and accounts for mass and heat transfer between two phases. The computational model utilizes an axisymmetric model, where the axis of symmetry is defined as the line that connects the centers of the particles and the bubble. A comprehensive analysis is presented on the influence of the particle radius and bubble–particle distance on the jet behavior. Furthermore, the variations of surface pressure on the particles induced by jet impingement are quantitatively analyzed. Four distinct jet behaviors are categorized, depending on the formation mechanism, as well as the number and the direction of the jets. For case 1, the bubble produces a single jet directed toward a small particle; for case 2, the bubble fragments produces double jets receding from each other; for case 3, the bubble produces double jets approaching each other; and for case 4, the bubble produces a single jet directed toward a large particle. The pressure perturbations induced by jet impingement upon the particles exceed those caused by shock wave impacts. The larger the bubble volume at the moment of jet formation, the longer the duration of the pressure variation caused by the jet impinging on the particles.

Keywords: jet dynamics; cavitation bubble dynamics; numerical simulation; cavitation bubble–particle interaction



Citation: Wang, Z.; Feng, Z.; Hu, J.; Zhang, Y.; Zhang, Y. Numerical Investigations on the Jet Dynamics during Cavitation Bubble Collapsing between Dual Particles. *Symmetry* **2024**, *16*, 535. <https://doi.org/10.3390/sym16050535>

Academic Editor: Theodore E. Simos

Received: 28 March 2024

Revised: 19 April 2024

Accepted: 23 April 2024

Published: 29 April 2024



Copyright: © 2024 by the authors. Licensee MDPI, Basel, Switzerland. This article is an open access article distributed under the terms and conditions of the Creative Commons Attribution (CC BY) license (<https://creativecommons.org/licenses/by/4.0/>).

1. Introduction

The interactions between particles and cavitation bubbles is a pivotal research focus across various disciplines, such as hydraulic engineering [1–4], biomedical science [5–7], and mineral flotation [8,9]. In practical scenarios within these fields, particles often exist not in isolation but rather as clusters or groups of particles. Consequently, the presence of multiple particles profoundly influences the behavior of bubble jets, rendering the investigation of bubble–multiparticle interactions more imperative than bubble–single-particle interactions. Therefore, the objective of the present paper is to investigate the interactions of a bubble with unequal-sized dual particles based on OpenFOAM, an open source code fluid dynamics simulation tool.

Prior investigations into particle–bubble interactions have predominantly focused on scenarios involving a single bubble interacting with either one or dual particles. For bubble–single-particle interactions, researchers initially explored the impact of a particle on the orientation and the morphology of bubble collapse. Xu et al. [10] investigated the impact of a single particle on the collapse orientation of a bubble generated by an electric

spark, and quantitatively determined the correlation between the bubble–particle distance and the orientation of bubble collapse. Chen et al. [11] explored the impact of particle shape—specifically a conical and cubical particle fabricated from anthracite—on the bubble behavior. They observed that the bubble tends to collide with and subsequently detach more readily from the apex of the particle.

Due to the rapid evolution of the jet, traditional experimental methods often fall short in elucidating the mechanisms behind jet generation and its effects on particles. Nevertheless, numerical simulation combining the finite volume method and the fluid volume method provides a powerful tool for revealing the jet formation mechanism [12,13]. Zevnik and Dular [14] simulated the bubble–single-particle interaction utilizing the finite volume method. Their simulations revealed that the surface pressure exerted on the particle increase with the particle–bubble radius ratio, while diminish with an increase in the particle–bubble distance. Dai et al. [15] conducted simulations to analyze the jet behaviors of a bubble near a single particle and distinguished three distinct patterns of jet behavior depending on the contact type between the jet and the particle. They further examined the particle–bubble distance effect on the jet velocity and the pressure on the particle. Lyu et al. [16] conducted a numerical analysis to investigate the influence of particle size and particle–bubble distance on bubble collapse behavior. Their findings indicate that an increase in the particle size or a reduction in the particle–bubble distance intensifies the collapse of the bubble, augmenting the asymmetry in the behavior of the collapsing bubble. Li et al. [17] performed a numerical investigation to examine the interaction between bubbles and suspended particles. They discovered that the jet velocity near suspended particles is greater compared to that around a stationary particle.

For interactions between a bubble and the dual particles, Chen et al. [18] executed an experimental investigation and observed that the characteristics of the bubble jets demonstrate marked symmetry when equal-sized particles are present. Conversely, when unequal-sized particles are present, the bubble jet is more likely to be directed toward the large particle. Hu et al. [19] elucidated the underlying cause of bubble fragmentation by conducting numerical simulations. Their findings indicate that the increasing and converging high-pressure liquid surrounding the middle of the bubble is the primary factor resulting in bubble fragmentation. Wang et al. [20] investigated the impact of unequal-sized dual particles on bubble collapse characteristics employing high-speed photography and the Kelvin impulse model. They commenced by corroborating the predictive capacity of the model for the displacement and direction of the bubble centroid utilizing experimental data. Their theoretical analysis disclosed that the ratio of particle radii is a pivotal factor influencing the strength and orientation of the Kelvin impulse. Chen et al. [21] examined the characteristics of bubble collapse near single and multiple particles. They observed that the collapse duration of the bubble near eight small particles is prolonged with a low collapse intensity compared to a single large particle.

Nonetheless, the understanding of the interactions between bubble jets and dual particles with unequal sizes remains limited. The mechanisms through which particle radius and particle–bubble distance influence the characteristics of bubble jets are not yet fully elucidated. Therefore, the objective of this paper is to investigate the evolutionary mechanism of the bubble jet near unequal-sized dual particles and its effect on the particles.

2. Numerical Method

2.1. Bubble–Unequal-Sized Dual Particles System

Figure 1 depicts a schematic diagram of the layout of the unequal-sized dual particles and the bubble. The particles are depicted as gray spheres, with the radius of the small particle denoted by R_S , and the large one as R_L (which is 2.0 mm in the current research). The bubble is depicted as a green sphere, with its centroid positioned on the line that connects the centroids of the two particles. The Cartesian coordinate system is established with the upper vertex of the large particle serving as the origin O . The vertical distance from the origin O to the bubble inception is labeled as d , while the vertical separation between

the upper vertex of the large particle and the lower vertex of the small particle is defined as D .

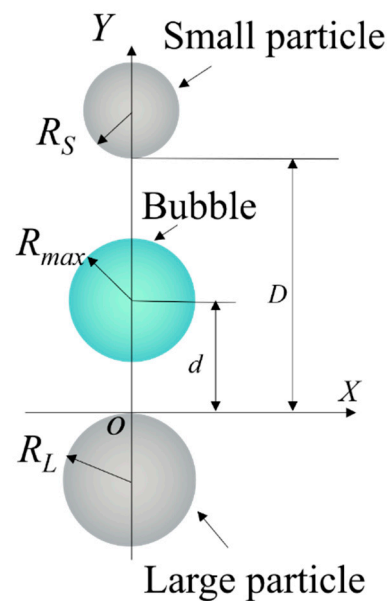


Figure 1. Schematic of the layout of the unequal-sized dual particles and the bubble.

For facilitate analysis, several dimensionless parameters are defined as follows:

$$\delta = \frac{R_L}{R_S} \quad (1)$$

$$\eta = \frac{R_L}{R_{max}} \quad (2)$$

$$\gamma = \frac{D}{R_{max}} \quad (3)$$

$$\gamma_L = \frac{d}{R_{max}} \quad (4)$$

$$\gamma_s = \frac{D - d}{R_{max}} \quad (5)$$

where R_{max} is the maximum radius of the bubble (being 1.0 mm), δ signifies the dimensionless ratio of the radii between the large and the small particles, η represents the dimensionless ratio of the radius of the large particle to R_{max} , γ denotes the dimensionless distance between two particles, γ_L represents the dimensionless distance between the location of bubble inception and the upper vertex of the large particle, and γ_s represents the dimensionless distance between the location of bubble inception and the lower vertex of the small particle.

2.2. Governing Equations

The bubble is assumed to be a pure vapor bubble, devoid of noncondensable gases, with the liquid and the vapor phases separated by an interface of finite thickness. During bubble oscillations, a substantial amount of energy is released, leading to the mass transfer and thermal diffusion of liquid and vapor across the bubble interface. Since the bubble size is in the micron or millimeter scale, the surface tension and the viscosity of the liquid significantly influence the dynamic behavior of the bubble. Consequently, the two-phase compressible solver compressibleVoF in OpenFOAM-11 [22] is utilized, which incorporates fluid compressibility, surface tension, viscosity, thermodynamic effects, and mass transfer. The solver discerns between liquids and vapors utilizing the volume of fluid (VOF) method.

In VOF, the density and viscosity of fluid are expressed as follows [23]:

$$\rho = \alpha_l \rho_l + \alpha_v \rho_v \quad (6)$$

$$\mu = \alpha_l \mu_l + \alpha_v \mu_v \quad (7)$$

with

$$\alpha_l + \alpha_v = 1 \quad (8)$$

where ρ , α , and μ represent the density, volume fraction, and viscosity of the fluid respectively. Subscripts (l for liquid and v for vapor) are utilized to differentiate the property parameters between the two phases.

The mass conservation equation, momentum conservation equation, and energy conservation equation for the solver are given as follows [23]:

$$\frac{\partial \rho}{\partial t} + \nabla \cdot (\rho \mathbf{U}) = 0 \quad (9)$$

$$\frac{\partial \rho \mathbf{U}}{\partial t} + \nabla \cdot (\rho \mathbf{U} \mathbf{U}) = -\nabla p + \mathbf{F}_s + \nabla \cdot \boldsymbol{\tau} \quad (10)$$

$$\frac{\partial \rho T}{\partial t} + \nabla \cdot (\rho \mathbf{U} T) + \left(\frac{\alpha_l}{C_{v,l}} + \frac{\alpha_v}{C_{v,v}} \right) \left[\frac{\partial \rho K}{\partial t} + \nabla \cdot (\rho \mathbf{U} K) \right] = \left(\frac{\alpha_l}{C_{v,l}} + \frac{\alpha_v}{C_{v,v}} \right) \left[\frac{\partial \rho}{\partial t} + \nabla \cdot (\mathbf{U} \rho) \right] + \left(\frac{\alpha_l \lambda_l}{C_{v,l}} + \frac{\alpha_v \lambda_v}{C_{v,v}} \right) (\nabla^2 T) \quad (11)$$

where \mathbf{U} , p , T , and K are the velocity, pressure, temperature, and kinematic energy of the fluid, respectively; \mathbf{F}_s is surface tension; $\boldsymbol{\tau}$ is viscous force tensor; and C_v and λ are the specific heat capacity and thermal conductivity of the fluid, respectively.

Based on the VOF, the mass conservation equations for each phase with mass transfer considered are [23]

$$\frac{\partial \alpha_l \rho_l}{\partial t} + \nabla \cdot (\alpha_l \rho_l \mathbf{U}) = +\dot{m} \quad (12)$$

$$\frac{\partial \alpha_v \rho_v}{\partial t} + \nabla \cdot (\alpha_v \rho_v \mathbf{U}) = -\dot{m} \quad (13)$$

where the mass transfer rate \dot{m} is solved by the Schnerr–Sauer cavitation model [24,25].

The phase equation is expressed as follows [23]:

$$\frac{\partial \alpha_l}{\partial t} + \nabla \cdot (\alpha_l \mathbf{U}) + \nabla \cdot (\alpha_l \alpha_v \mathbf{U}_r) = \alpha_l \alpha_v \left(\frac{\psi_v}{\rho_v} - \frac{\psi_l}{\rho_l} \right) \frac{Dp}{Dt} + \dot{m} \left[\frac{1}{\rho_l} - \alpha_l \left(\frac{1}{\rho_l} - \frac{1}{\rho_v} \right) \right] + \alpha_l \nabla \cdot \mathbf{U} \quad (14)$$

where $\psi = d\rho/dp$ is the compressibility of fluid and \mathbf{U}_r represents the relative velocity of the two phases [26].

The growth and collapse of a cavitation bubble causes significant variations in the local fluid pressure and temperature. Therefore, the fluid density is affected by both pressure and temperature. The equations of state for liquid and vapor are given as follows [27]:

$$\rho_l = \frac{p + p_l}{K_l(T + T_l)} \quad (15)$$

$$\rho_v = \frac{p}{R_v T} \quad (16)$$

where p_l , K_l , and T_l are the pressure constant, liquid constant, and temperature constant of water, respectively, and R_v is the vapor constant.

2.3. Numerical Implementation

Figure 2 shows the computing domain and grid for simulating interactions between a bubble and unequal-sized dual particles. As depicted in Figure 2a, an axisymmetric computing domain is adopted depending on the layout of the bubble and the dual particles. The centers of both particles, as well as the center of the bubble, are positioned along the

axis of symmetry (e.g., Y -axis). Consequently, the entire computing domain takes the form of a hemispherical wedge, with its center at the upper vertex of the large particle. The domain has a radius of $60 R_{max}$ and a wedge angle of 5° .

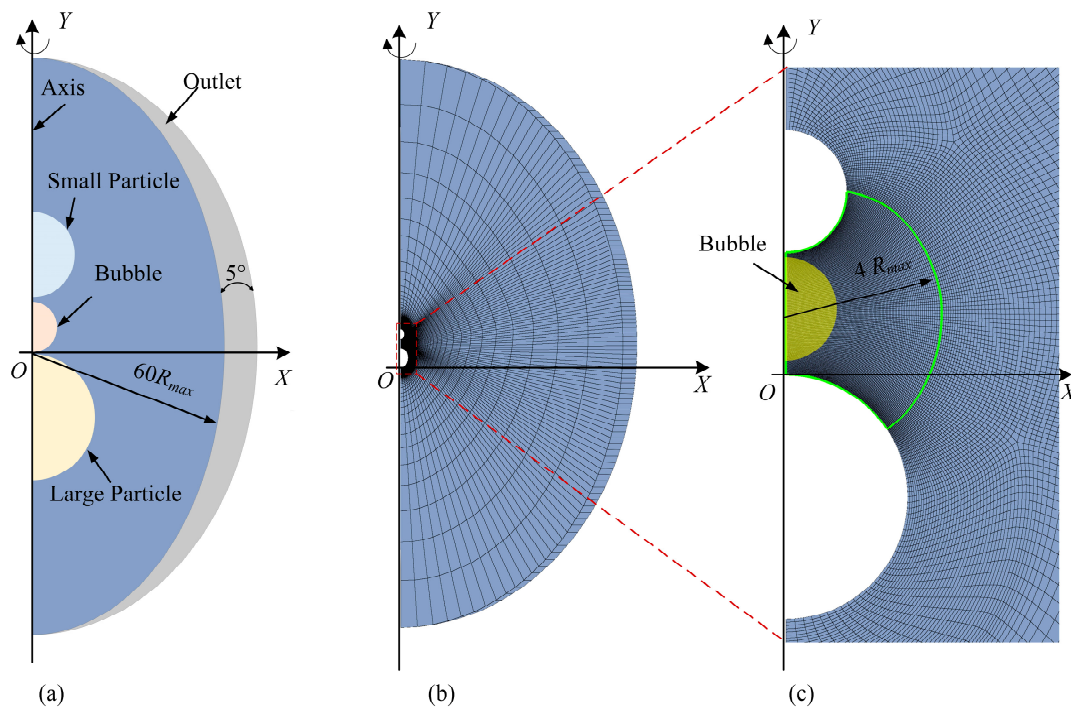


Figure 2. Computing domain and grid for simulating the interactions between the bubble and unequal-sized dual particles: (a) computing domain; (b) grid for the entire computing domain; (c) zoomed-in view of the grid in the region of the bubble–particle interactions.

Figure 2b illustrates the structured grid in the computing domain. Figure 2c presents a zoomed-in view of the grid in the region of the bubble–particle interactions. In Figure 2c, the grid within the region (formed by the four green lines) near the particles and the bubble is refined to accurately track the variations of the bubble interface. The size of the grid cells within the refined region is managed by adjusting the number of nodes along the four green lines. According to our previous work [19], the accuracy and efficiency of the simulations demonstrate a great balance at a minimum grid size of $2.4 \mu\text{m}$. The rate of grid expansion outside the refined region is set at a factor of 1.25.

The generation of a bubble is a complex process that falls outside the scope of the current research. Therefore, the interactions between the bubble and the particles are simulated from the state shortly after bubble inception. Specifically, an initial bubble shape is modeled as a hemispherical region (yellow region in Figure 2c) with a radius of 0.2 mm , and high temperature and pressure are applied to drive the bubble growth. The surfaces of both particles are treated as walls, and the outlet is set as a boundary condition that will not reflect the wave. The numerical schemes employed and the solvers adopted for the coefficient matrix are consistent with those from our previous research [19].

3. Experimental Verification with a Laser-Induced Cavitation Bubble

Figure 3 presents a comparison between the experimental results and simulations. Figure 3a,b illustrate the variations in bubble shape from the experiments and simulations, respectively. The number in the lower left corner of each subgraph is the number of each frame. Figure 3c contrasts the displacements of feature points in both the experiments and simulations.

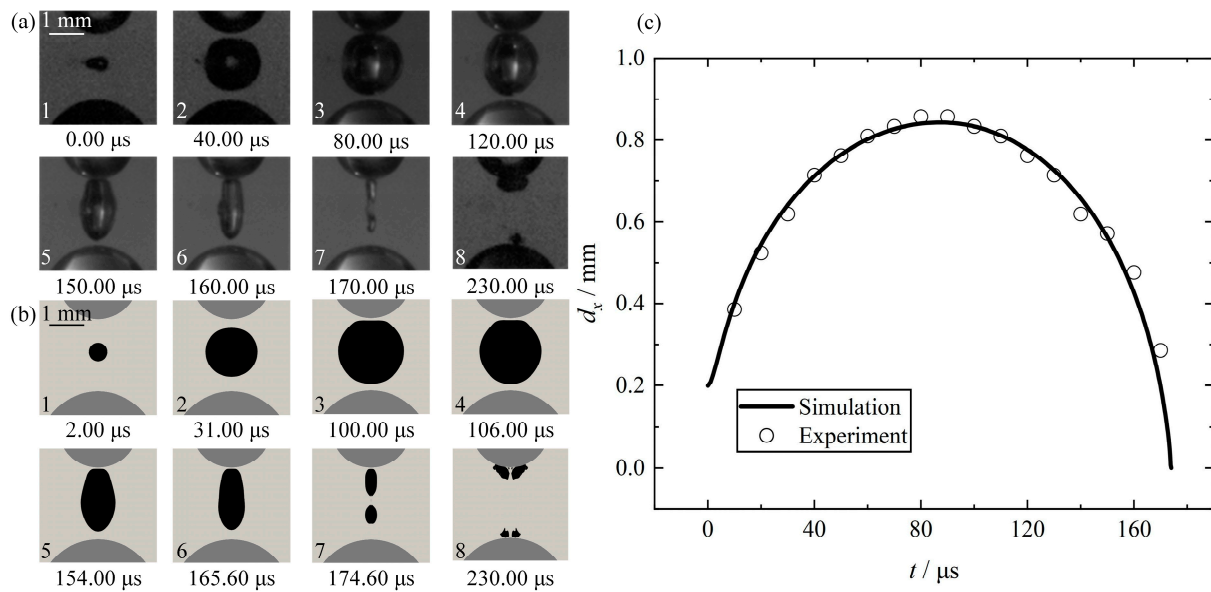


Figure 3. Qualitative and quantitative comparison of the simulation results with the experimental results: (a) experimental results; (b) simulation results; (c) quantitative comparison of experiments and simulations. The gray and black regions in the simulation results represent the liquid and the bubble, respectively. The dark gray regions represent the particles, respectively. $R_L = 1.50 \text{ mm}$, $R_S = 1.00 \text{ mm}$, $d = 0.96 \text{ mm}$, $D = 1.78 \text{ mm}$.

The experimental setup is consistent with our previous research regarding bubble dynamics in the vicinity of equal-sized dual particles [19]. The experimental methodology is briefly described below. The experiments are conducted in a transparent acrylic square tank filled with deionized water. Particles are fixed on a needle tip, which is attached to a micrometric XYZ-axis displacement slide stage. With the water in the tank at rest, a laser beam from a laser generator is focused to a constant position in the water, causing the ionization of the water molecules, and the formation of a bubble. The high-speed camera is employed to capture bubble pictures.

In Figure 3a,b, during the bubble growth stage (from frames 1 to 3), the proximity of the bubble inception site to the small particle causes the upper portion of the bubble to progressively envelop the small particle. During bubble collapse stage (frames 4 to 8), the bubble fragments into two parts as the middle portion of the bubble contracts along the axis of symmetry. The upper sub-bubble collapses along the surface of the small particle, while the lower sub-bubble moves toward the large particle. In Figure 3c, d_x denotes the distance between the Y-axis and the feature point on the bubble interface. The feature point is the intersection of the horizontal plane at $Y = 0.96 \text{ mm}$ with the bubble interface. From the variations in bubble morphology and feature point over time, it is evident that the results forecasted by the numerical solver are consistent with experimental findings.

4. Typical Jet Behaviors near Unequal-Sized Dual Particles

Based on the quantity and the direction of jets, the observed jet behaviors in the simulations could be categorized into four cases. Table 1 summarizes the principal features of these jet behaviors. For case 1, the small particle exerts a significant influence on the bubble, causing a jet to form toward the small particle. For case 2, the bubble fragments into two sub-bubbles of unequal size, generating two jets that recede from each other. For case 3, two jets approaching each other are formed inside the bubble, causing the bubble to adopt an annular shape after they encounter. For case 4, the large particle significantly affects the bubble, producing a jet directed toward the large particle.

Table 1. Principal features of jet behaviors for four cases.

Cases	No. of Jets	Orientation
1	1	Toward the small particle
2	2	Receding each other
3	2	Approaching each other
4	1	Toward the large particle

Figures 4–7 depict the jet evolution for each of the four cases during the bubble collapse stage. Each frame is divided into two sections: the left panel illustrates the pressure contours and the right panel reveals the velocity contours. The arrow in the velocity distribution indicates the orientation of the liquid. The two gray regions represent the particles and the white region signifies the bubble. The following is a detailed description of the evolution of the jets for the four cases.

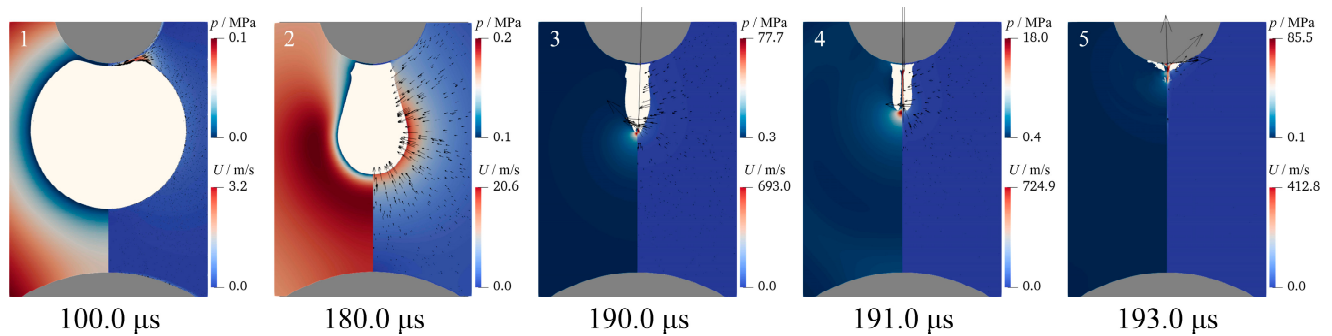


Figure 4. Jet evolution for case 1. The left panel of each frame presents the pressure contours and the right panel indicates the velocity contours. The two gray regions represent the particles and the white region signifies the bubble. $\delta = 3.0$, $\gamma = 2.5$, $\gamma_L = 1.7$, $\eta = 2.0$.

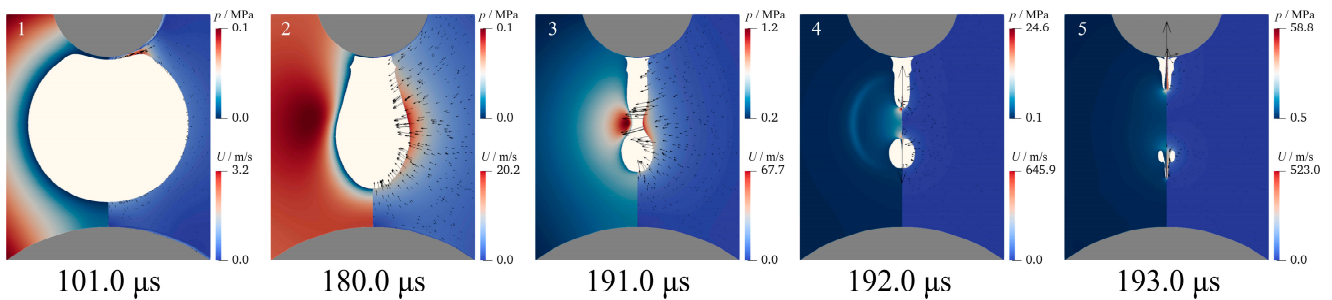


Figure 5. Jet evolution for case 2. The left panel of each frame presents the pressure contours and the right panel indicates the velocity contours. The two gray regions represent the particles and the white region signifies the bubble. $\delta = 3.0$, $\gamma = 2.0$, $\gamma_L = 1.2$, $\eta = 2.0$.

Figure 4 delineates the jet evolution for case 1. In frame 1, when the bubble attains its maximum volume, its upper envelope the lower surface of the small particle, resulting in the generation of a thin liquid film between them. Concurrently, the lower portion of the bubble still maintains a distance from the large particle, preserving its spherical shape. As the bubble begins to contract, frames 2 and 3 reveal the upper portion of the bubble collapsing along the lower surface of the small particle, while the lower portion contracts spherically. The pressure of the liquid underneath the bubble progressively rises, and converges near the axis of symmetry. In frame 4, the liquid underneath the bubble induces a depression on the bubble interface, which subsequently forms a high-velocity jet directed toward the small particle. Finally, in frame 5, the jet arrives the surface of the small particle, and the bubble continues to shrink until it collapses. During bubble collapse, the proximity

of the small particle to the bubble prevents the upper portion of the bubble from contracting toward its center, leading to an elongation of the bubble.

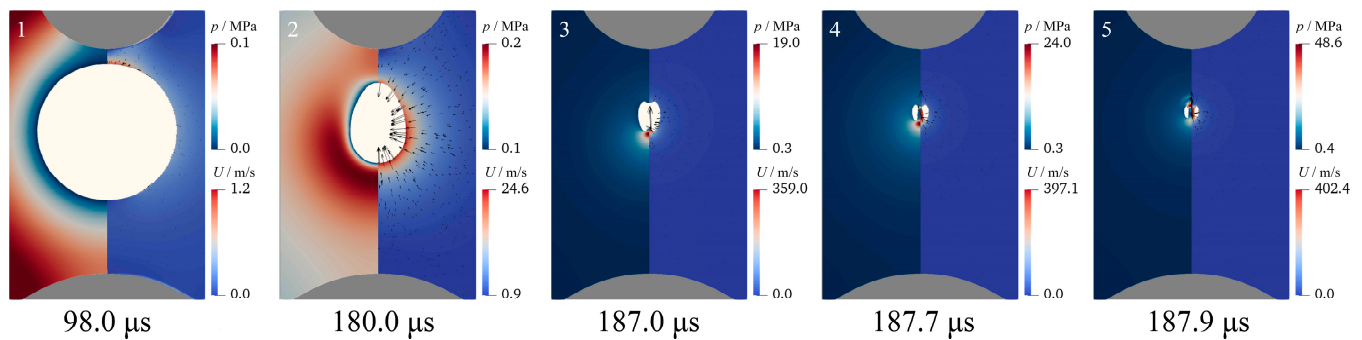


Figure 6. Jet evolution for case 3. The left panel of each frame presents the pressure contours and the right panel indicates the velocity contours. The two gray regions represent the particles and the white region signifies the bubble. $\delta = 2.0$, $\gamma = 3.0$, $\gamma_L = 1.9$, $\eta = 2.0$.

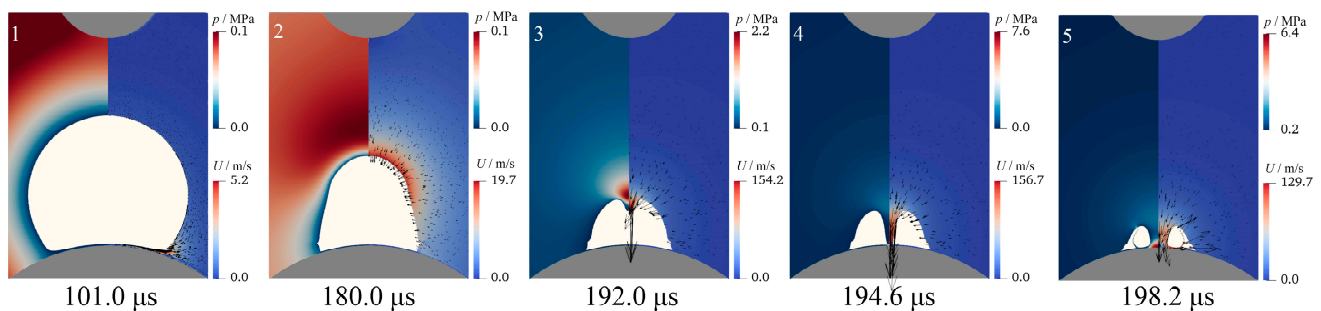


Figure 7. Jet evolution for case 4. The left panel of each frame presents the pressure contours and the right panel indicates the velocity contours. The two gray regions represent the particles and the white region signifies the bubble. $\delta = 3.0$, $\gamma = 2.5$, $\gamma_L = 0.6$, $\eta = 2.0$.

Figure 5 delineates the jet evolution for case 2. When the bubble attains its maximum volume (frame 1), it exhibits a shape similar to those in frame 1 of Figure 4. In frames 2 and 3, the upper portion of the bubble contracts along the surface of the small particle. The lower portion of the bubble is restrained by the large particle, causing a slow contraction toward the center of the bubble. With the dual confinement of the two particles, the liquid pressure surrounding the upper and the lower portions of the bubble is reduced, which slows the rate of bubble contraction and leads to an elongation of the bubble. The high-pressure liquid around the middle of the bubble causes the bubble interface to contract rapidly. Therefore, in frame 4, as the middle of the bubble contracts to the axis of symmetry, the bubble fragments and generates a high-pressure liquid near the fragmentation point. The high-pressure liquid causes each sub-bubble to produce a jet. In frame 5, the jet inside the upper sub-bubble impinges on the surface of the small particle, and the jet inside the lower sub-bubble penetrates the bubble interface and advances toward the large particle.

Figure 6 illustrates the jet evolution for case 3. In frame 1, the distance between the bubble and both particles are large, with the bubble positioned closer to the small particle. The gradient of liquid pressure from the middle of the bubble toward the large particle is greater than that toward the small particle, causing an inhomogeneous contraction rate of the bubble interface. Such inhomogeneity causes the bubble to be elongated in the vertical direction (frame 2). From frame 2 to frame 3, the lower portion of the bubble contracts rapidly due to the large liquid pressure gradient. As the bubble continues to contract, the high-pressure liquid converges toward the axis of symmetry, leading to the generation of a jet directed at the small particle. Concurrently, the upper portion of the bubble also forms a jet, which is slowly moving and oriented toward the large particle. In frame 4, the

interaction of the double jets results in the bubble evolving into a ring shape. Finally, in frame 5, the ring-shaped bubble continues its trajectory toward the small particle.

Figure 7 demonstrates the jet evolution for case 4. In frame 1, the bubble is positioned further from the small particle and envelops the upper surface of the large particle, with its upper portion maintaining a spherical shape. The gradient of liquid pressure around the bubble increases from the lower portion of the bubble to the upper portion. Consequently, in frame 2, the bubble elongates vertically. From frame 2 to frame 3, the upper portion of the bubble contracts rapidly due to a high liquid pressure, while the lower part contracts slowly along the surface of the large particle. High-pressure liquid converges toward the top of the bubble, forming a depression and subsequently generating a jet. In frames 4 and 5, this jet directed at the large particle penetrates through the bubble interface and ultimately impacts the surface of the large particle.

5. Influencing Parameters on the Bubble Jets

5.1. Case 1

Figure 8 illustrates the evolution of the jet for case 1. Three distinct data sets for δ , γ , and γ_L are chosen to demonstrate the influence of the particle radius and particle–bubble distance on jet behavior. In Figure 8a, the proximity of the bubble to the small particle results in its upper portion enveloping a section of the small particle, while its lower portion remains spherical. In frame 2, as the bubble contracts, the bubble develops a distinct neck structure. Owing to the significant influence of the small particle and the minimal effect of the large one, the shape of the bubble resembles that near a single particle, taking on a mushroom-like form [15]. In frame 3, the velocity and the pressure of the liquid surrounding the neck increase. In frame 4, when the neck contracts along the axis of symmetry, it generates a high-pressure liquid region and excites a shock wave. The high-pressure liquid exerts on the bubble bottom, leading to the generation of a jet toward the small particle. In frame 5, the jet impacts the surface of the small particle.

In Figure 8b, the increase in the radius of the small particle causes the formation mechanism of the jet to be different from Figure 8a. The pressure of liquid underneath the bubble progressively increases and concentrates toward the bubble bottom. The concentrated high-pressure liquid induces the bubble to produce a jet oriented toward the small particle.

In Figure 8c, the spacing between the two particles decreases, and the radius of the small particle increases again. In frame 1, the bubble is generated close to the large particle, resulting in a large contact area with the large particle compared to the small particle. In frame 2, the upper portion of the bubble contracts slowly along the surface of the small particle, while the lower portion of the bubble contracts rapidly along the surface of the large particle. Consequently, in frames 3 and 4, the interface of the lower portion of the bubble contracts to the axis of symmetry, generating a jet directed toward the small particle and simultaneously exciting a shock wave.

Figure 9 depicts the temporal variation of pressure on the particles for case 1 with different values of δ , γ , and γ_L . Each subplot is a counterpart to the corresponding case in Figure 8. To analyze the interaction between the particles and the bubble, a specific point on each particle was chosen. For the large particle, the point of interest is its upper vertex, represented by the black curve. For the small particle, the point of interest is its lower vertex, represented by the red curve. The details in the blue boxes are enlarged to clearly show the pressure variations.

In Figure 9a, the impact of the jet on the small particle causes an abrupt rise in surface pressure. As the high-velocity liquid within the jet continues to impact the particle surface, the surface pressure progressively decreases with dramatic fluctuations. In contrast, the large particle exhibits significantly milder surface pressure fluctuations compared to the small particle. The pressure variations observed on the large particle are induced by the shock wave generated as the jet impinges on the small particle.

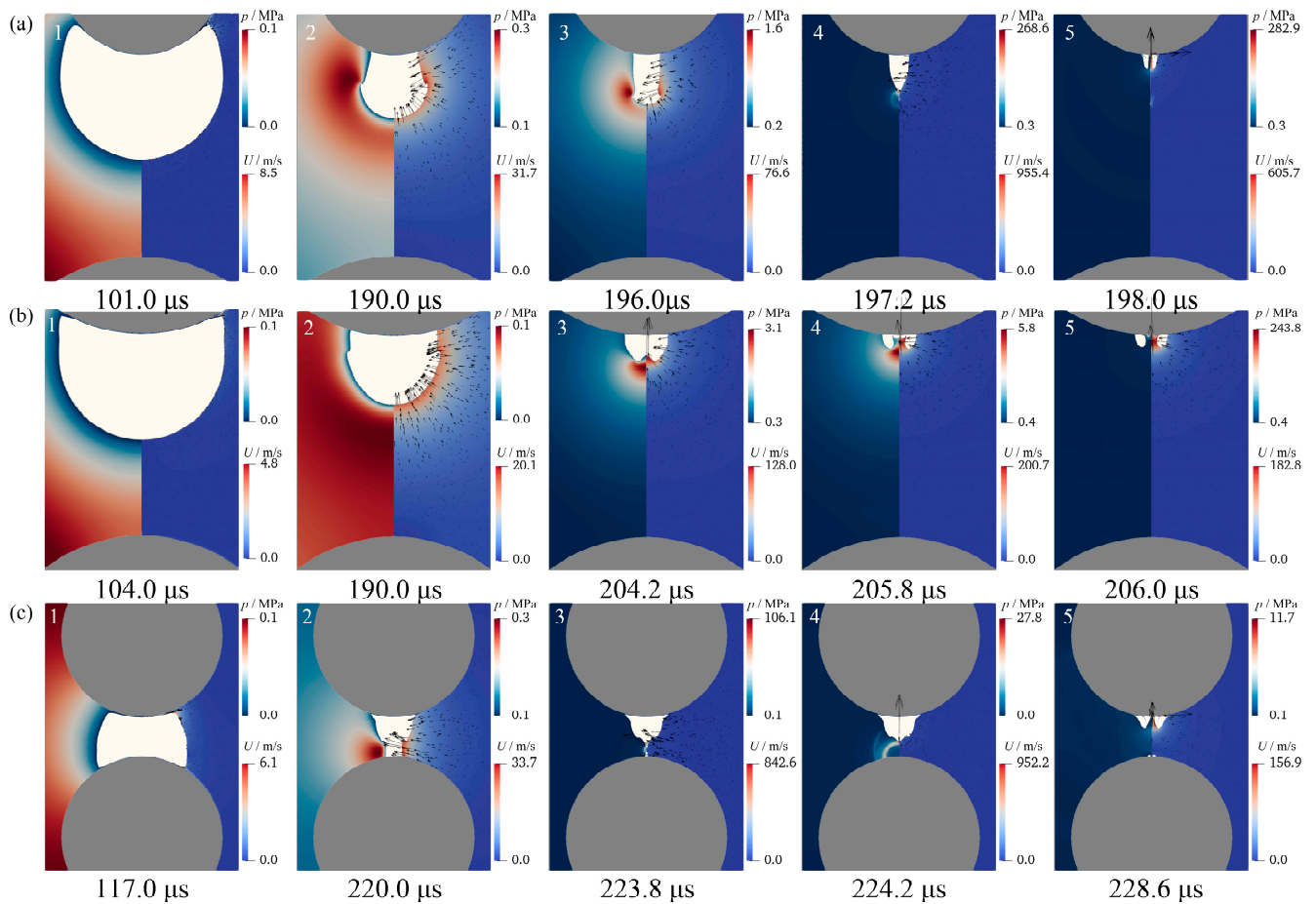


Figure 8. Jet evolution for case 1 with different values of δ , γ and γ_L . The left panel of each frame presents the pressure contours and the right panel indicates the velocity contours. The two gray regions represent the particles and the white region signifies the bubble: (a) $\delta = 2.0$, $\gamma = 2.5$, $\gamma_L = 2.2$; (b) $\delta = 1.0$, $\gamma = 2.5$, $\gamma_L = 2.2$; (c) $\delta = 1.0$, $\gamma = 1.0$, $\gamma_L = 0.3$, $\eta = 2.0$.

In Figure 9b, for the small particle, the pressure profile exhibits two distinct types of fluctuations. The first fluctuation is attributable to the direct impact of the jet on the particle surface, while the second is the consequence of the bubble collapse. For the large particle, the variations in particle surface pressure are driven by similar mechanisms to those described in Figure 9a.

In Figure 9c, the surface pressures on the two particles exhibit distinct variations. Temporally, the onset of increased pressure for the large particle precedes that of the small particle. In terms of the magnitude of the pressure increase, the surface pressure of the large particle increases significantly more than that of the small particle. Regarding the duration of the pressure increase, the period of increased surface pressure for the large particle is considerably shorter than that experienced by the small particle. These differences are attributed to the fact that the bubble interface first contracts to the axis of symmetry near the large particle before generating a jet toward the small particle.

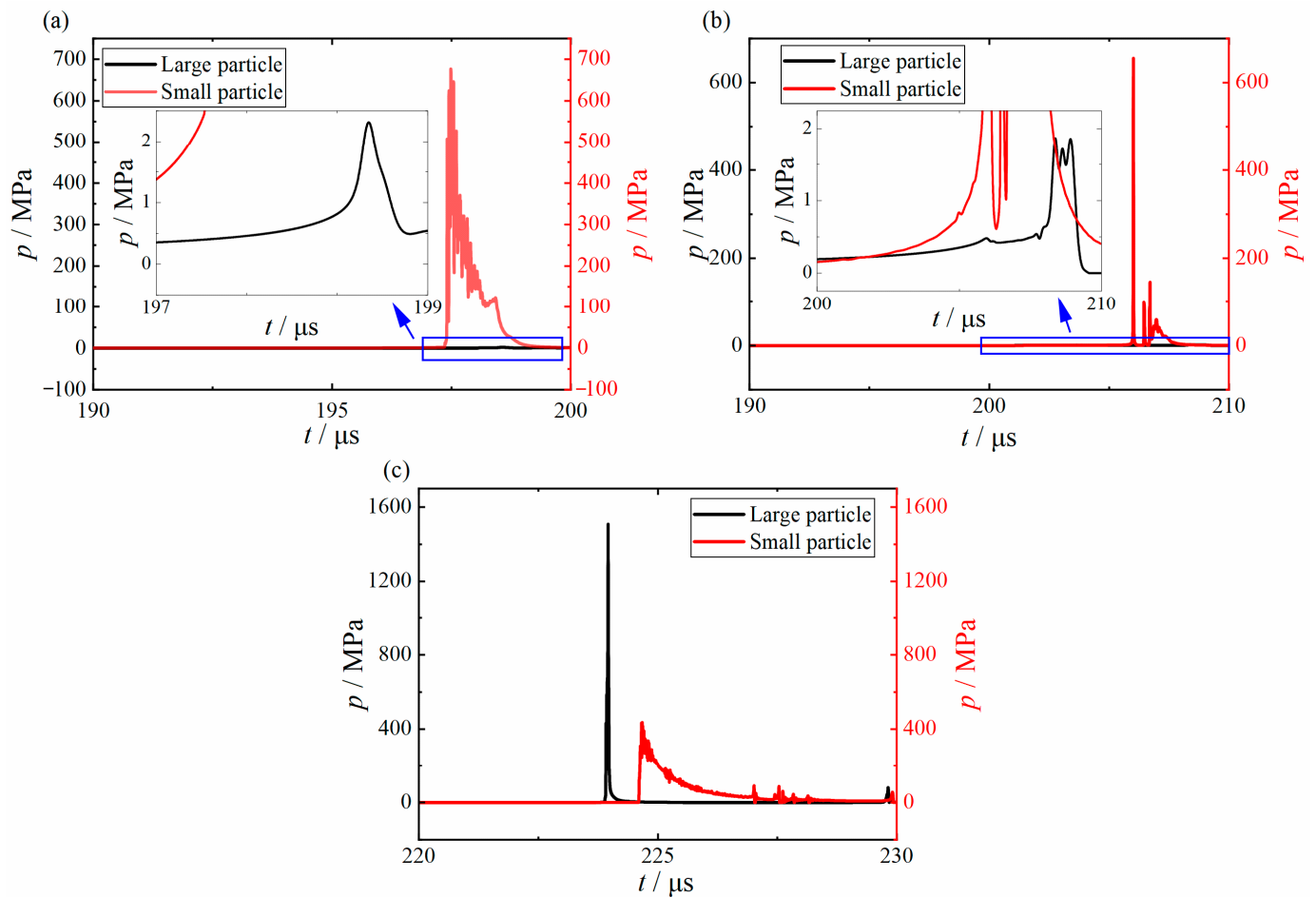


Figure 9. Temporal variation of surface pressure on the particles for case 1. The red curve depicts the pressure variations at the lower vertex of the small particle and the black curve depicts the pressure variations at the upper vertex of the large particle: (a) $\delta = 2.0$, $\gamma = 2.5$, $\gamma_L = 2.2$; (b) $\delta = 1.0$, $\gamma = 2.5$, $\gamma_L = 2.2$; (c) $\delta = 1.0$, $\gamma = 1.0$, $\gamma_L = 0.3$, $\eta = 2.0$.

5.2. Case 2

Figure 10 illustrates the evolution of the jet for case 2. Three distinct data sets for δ , γ , and γ_L are chosen to demonstrate the influence of the particle radius and particle–bubble distance on jet behavior.

In Figure 10a, the proximity of the bubble to the small particle is minimal, whereas its distance from the large particle is considerable. Consequently, the upper portion of the bubble envelops a segment of the small particle, while its lower portion retains a spherical shape. From frames 2 to 3, a neck forms during the collapse of the bubble. The pressure and the velocity of the liquid decrease progressively from the neck to both the lower and the upper portions of the bubble. As a result, in frame 4, the neck contracts along the axis of symmetry and the bubble fragments, evolving into two sub-bubbles. Simultaneously, a high-pressure liquid is generated from the bubble fragmentation and a shock wave is excited. After the high-pressure liquid exerts on the two sub-bubbles, a jet form within each. The lower sub-bubble, being smaller, collapses more rapidly, followed by the collapse of the upper sub-bubble.

In Figure 10b, the bubble is in close proximity to both particles, resulting in the bubble enclosing a portion of each particle at its maximum volume. During the bubble contraction, due to the short distance between the bubble and the large particle, the lower portion of the bubble contracts more slowly compared to the upper portion. The liquid pressure around the middle of the bubble continues to increase, pushing the middle of the bubble toward the axis of symmetry. The bubble splits along the axis of symmetry, resulting in

the formation of two sub-bubbles. The lower sub-bubble exhibits a large size compared to the upper one. Following the bubble fragmentation, two jets are produced within the sub-bubbles, moving in opposite directions away from each other and penetrating the bubble to impact the surface of particles. Meanwhile, owing to the large size of the lower sub-bubble, it collapses later than the upper one.

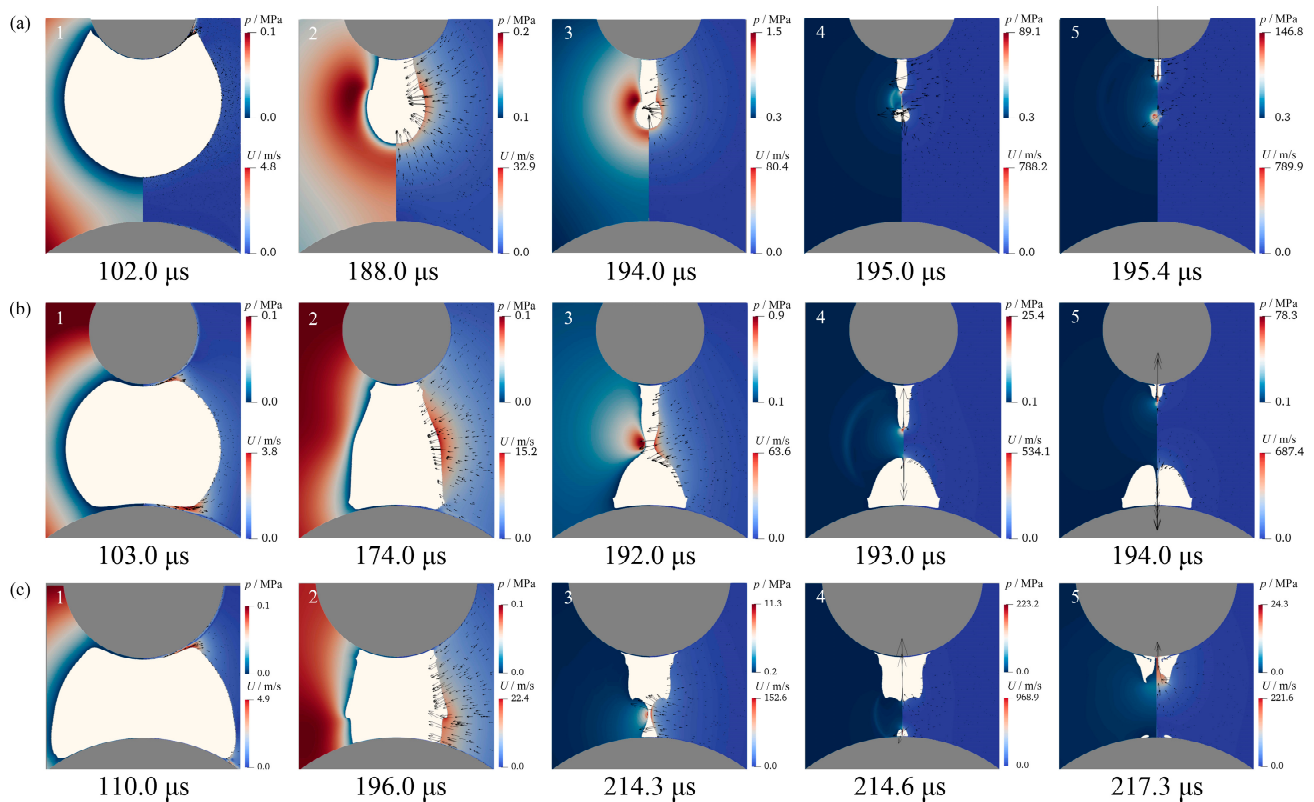


Figure 10. Jet evolution for case 2 with different values of δ , γ and γ_L . The left panel of each frame presents the pressure contours and the right panel indicates the velocity contours. The two gray regions represent the particles and the white region signifies the bubble: (a) $\delta = 3.0$, $\gamma = 2.0$, $\gamma_L = 1.5$; (b) $\delta = 3.0$, $\gamma = 1.5$, $\gamma_L = 0.7$; (c) $\delta = 2.0$, $\gamma = 1.0$, $\gamma_L = 0.2$, $\eta = 2.0$.

In Figure 10c, the relative positioning of the particles differs from that in Figure 10a,b, with a decreased distance between them and an increased size of the small particle. As a result, the bubble interface adjacent to the large particle develops a neck. During the progression from frames 2 to 3, the neck constricts more rapidly than the upper and the lower portion of the bubble. The neck contraction along the axis of symmetry eventually results in the generation of two sub-bubbles. Contrary to Figure 10b, the lower sub-bubble is smaller compared to the upper sub-bubble. Akin to Figure 10a,b, two jets are produced at the point where the bubble fragments, moving in opposite directions away from each other. Compared to the splitting behaviors of a bubble situated between equal-sized dual particles examined by Hu et al. [19], variations in the distance of the bubble from each particle and the disparity in the radii of the two particles result in the bubble-splitting event occurring close to one of the particles.

Figure 11 illustrates the temporal variation of pressure on the particles for case 2 with different values of δ , γ , and γ_L . Each subplot is a counterpart to the corresponding case in Figure 10. The details in the blue boxes are enlarged to clearly show the pressure variations.

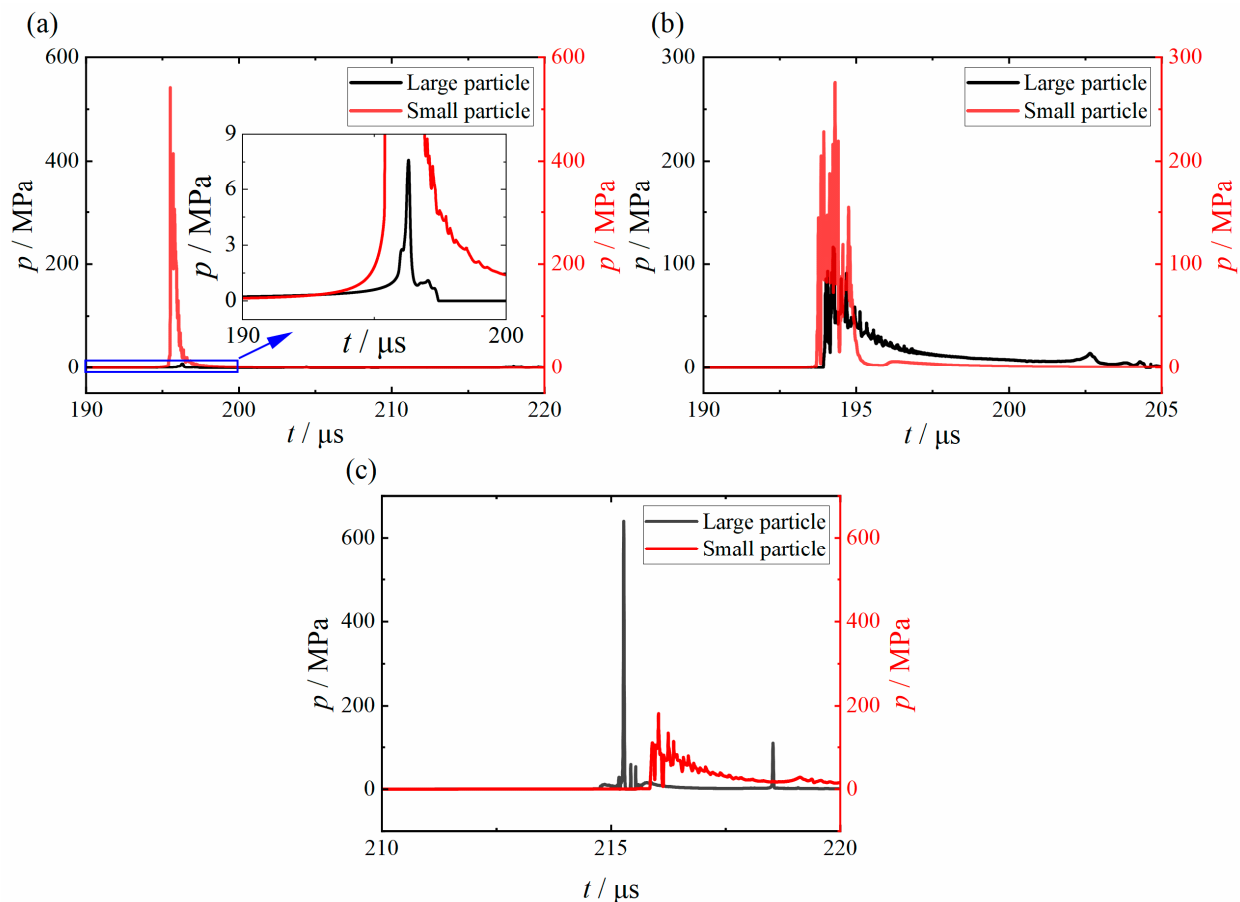


Figure 11. Temporal variation of surface pressure on the particles for case 2. The red curve depicts the pressure variations at the lower vertex of the small particle and the black curve depicts the pressure variations at the upper vertex of the large particle: (a) $\delta = 3.0$, $\gamma = 2.0$, $\gamma_L = 1.5$; (b) $\delta = 3.0$, $\gamma = 1.5$, $\gamma_L = 0.7$; (c) $\delta = 2.0$, $\gamma = 1.0$, $\gamma_L = 0.2$, $\eta = 2.0$.

In Figure 11a, the peak pressure on the surface of the small particle is considerably higher than that on the large particle. From Figure 10a, it is evident that the jet directly impacts the small particle without impacting the large particle. The pressure variations on the large particle are a result of the shock wave induced by the collapse of the lower sub-bubble, hence the significant difference in pressure variations on the surfaces of the two particles.

In Figure 11b, three distinct differences are observed in the pressure changes on the surfaces of the two particles. First, the increase in pressure on the small particle is more pronounced compared to that on the large particle. Second, the onset of pressure increase on the small particle occurs earlier than that on the large particle. Lastly, the duration of the pressure variation on the small particle is shorter than that experienced by the large particle. These disparities in pressure variations can be elucidated by the generation and evolution of the jets as depicted in Figure 10b. When the double jets formed, the sub-bubble adjacent to the small particle is small in size. Consequently, its jet reaches the small particle rapidly, and it collapses more rapidly than the sub-bubble near the large particle.

In Figure 11c, the proximity of the fragmentation location to the large particle results in substantial pressure increases on the large particle due to the jet impacts and the bubble collapse. Conversely, the jet directed toward the small particle requires a long time to reach the particle, which leads to a small magnitude of pressure increase but with a more extended duration compared to the large particle.

5.3. Case 3

Figure 12 illustrates the evolution of the jet for case 3. Two distinct data sets for δ , γ , and γ_L are chosen to demonstrate the effect of the particle radius and particle–bubble distance on jet behavior.

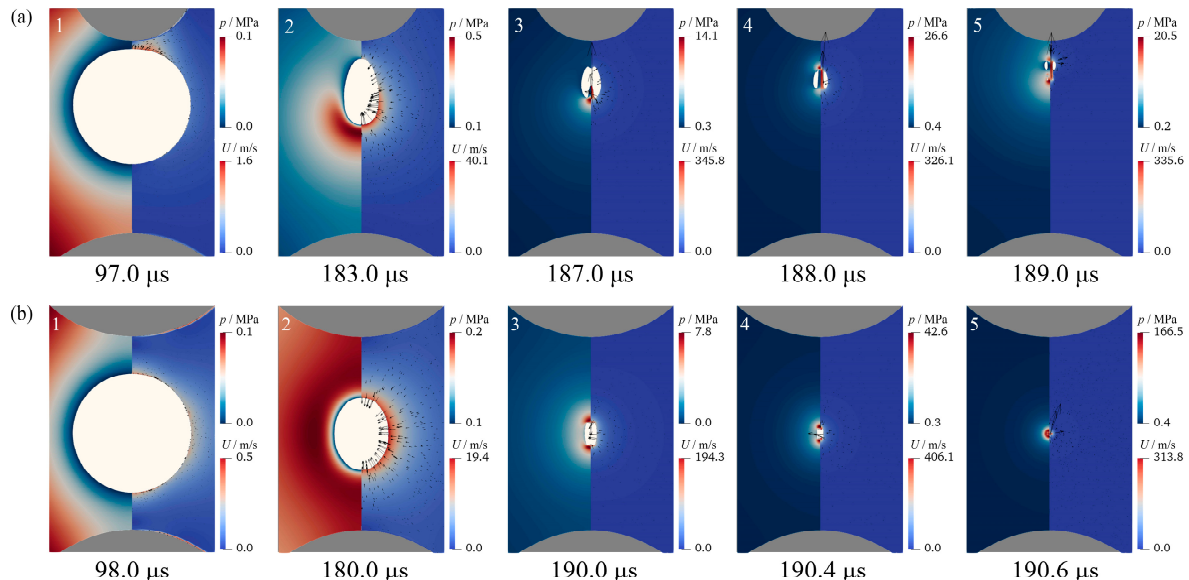


Figure 12. Jet evolution for case 3 with different values of δ , γ and γ_L . The left panel of each frame presents the pressure contours and the right panel indicates the velocity contours. The two gray regions represent the particles and the white region signifies the bubble: (a) $\delta = 2.0$, $\gamma = 3.0$, $\gamma_L = 2.0$; (b) $\delta = 1.0$, $\gamma = 3.0$, $\gamma_L = 1.5$, $\eta = 2.0$.

In Figure 12a, the bubble is situated near the small particle and at a considerable distance from the large particle, without making contact with either. In frames 2 to 3, the progressive increase in liquid pressure underneath the bubble results in the formation of a jet directed toward the small particle. Simultaneously, the upper portion of the bubble generates a jet toward the large particle. In frame 4, the two jets approaching each other meet and penetrate the bubble. The jet directed toward the small particle exhibits a high velocity, causing the bubble to be displaced toward the small particle. The high-pressure liquid generated at the puncture location will move toward the small particle, causing an increase in particle surface pressure. Wang et al. [20] observed a similar bubble shape evolution by employing laser-induced bubble experiments coupled with high-speed photography. According to the numerical simulation results in the present paper, the liquid pressure gradient around the bubble promotes the bubble-shape evolution.

In Figure 12b, the two particles are equal in radius, and the bubble is situated equidistantly between them. Consequently, the upper and the lower parts of the bubble illustrate the same process and mechanism of evolution. In frames 2 and 3, the pressure of the liquid above and below the bubble progressively increase in concentration near the axis of symmetry. Consequently, two jets of equal velocity and opposite direction form at the poles of the collapsing bubble. In frame 5, as the bubble collapses, it generates a high-pressure liquid at the point of collapse that subsequently spreads outward in the form of a shock wave.

Figure 13 illustrates the temporal variation of pressure on the particles for case 3 with different values of δ , γ , and γ_L . Each subplot is a counterpart to the corresponding case in Figure 12.

In Figure 13a, the peak pressure on the surface of the small particle is notably greater than that on the surface of the large particle. Furthermore, the period during which the pressure increases on the small particle is longer compared to that on the large particle. The difference in pressure dynamics can be attributed to the bubble's closer proximity to the

small particle, as well as the convergence of the double jets occurring near the small particle. Consequently, the jets and the subsequent shock wave initially reach the small particle, while the shock wave causes a less magnitude of pressure variation on the large particle.

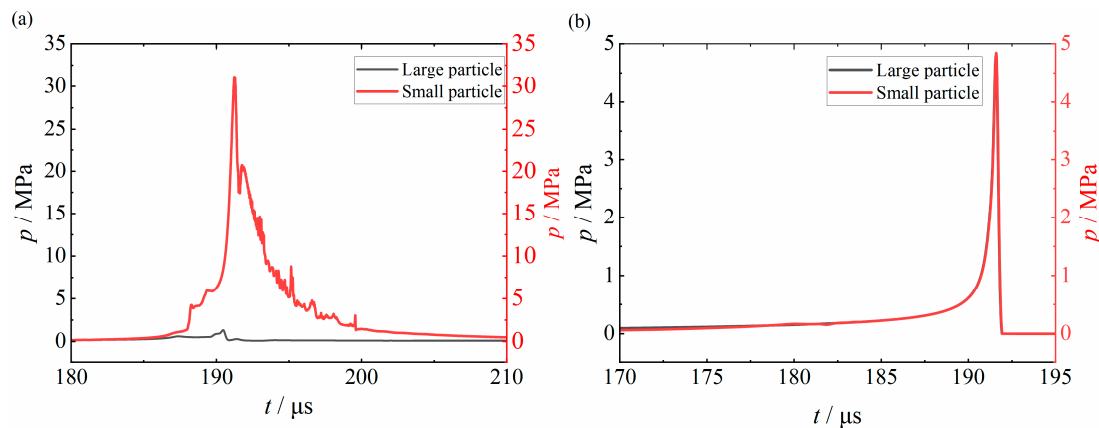


Figure 13. Temporal variation of surface pressure on the particles for case 3. The red curve depicts the pressure variations at the lower vertex of the small particle and the black curve depicts the pressure variations at the upper vertex of the large particle: (a) $\delta = 2.0$, $\gamma = 3.0$, $\gamma_L = 2.0$; (b) $\delta = 1.0$, $\gamma = 3.0$, $\gamma_L = 1.5$, $\eta = 2.0$.

In Figure 13b, owing to the symmetrical generation and evolution of the double jets, the pressure variations on both particles are identical. The pressure variations are both elicited by the shock wave that arises from the bubble collapse.

5.4. Case 4

Figure 14 illustrates the evolution of the jet for case 4. Three distinct data sets for δ , γ , and γ_L are chosen to demonstrate the influence of the particle radius and particle–bubble distance on jet behavior.

In Figure 14a, the bubble approaches the small particle and stays distant from the large particle, resulting in the upper portion of the bubble enveloping nearly half of the small particle, while the lower portion retains a spherical shape. As the bubble collapses, as shown in frame 2, it develops a neck adjacent to the small particle. The high-pressure liquid near the neck forces the bubble interface to constrict along the surface of the small particle. As the neck further constricts along the axis of symmetry (frames 3 and 4), a jet is produced toward the large particle, and a shock wave is excited. Subsequently, the jet penetrates the bubble interface and propels the bubble into the large particle.

In Figure 14b, the spacing between the two particles decreases compared to Figure 14a. As the bubble expands to its peak volume, it envelops the small particle at its upper portion and the large particle at its lower portion. Frames 2 to 3 reveal a consistent mechanism of jet formation as observed in Figure 14a. Following the formation of the jet, it penetrates the bubble and directly impacts the large particle.

Figure 14c exhibits a jet formation process analogous to that observed in Figure 14b. The distinction is noted in the morphology and dimensions of the bubble at the moment of jet generation.

Figure 15 presents the temporal variation of pressure on the particles for case 3 with different values of δ , γ , and γ_L . Each subplot is a counterpart to the corresponding case in Figure 14. The three data sets illustrate a consistent trend in the surface pressure variations on both particles. The increase in surface pressure is more pronounced on the small particle compared to the large particle. Additionally, the onset of pressure increase on the small particle occurs earlier, and its duration is shorter than that experienced by the large particle. The distinctions among the data sets are detailed as follows.

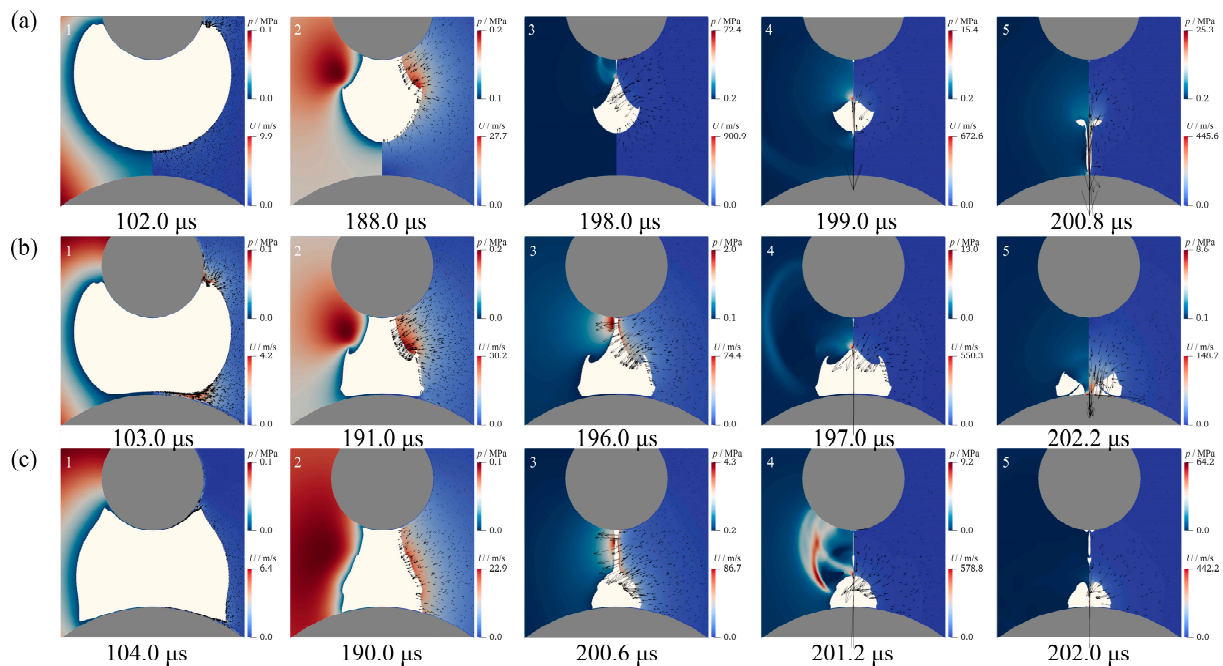


Figure 14. Jet evolution for case 4 with different values of δ , γ , and γ_L . The left panel of each frame presents the pressure contours and the right panel indicates the velocity contours. The two gray regions represent the particles and the white region signifies the bubble: (a) $\delta = 3.0$, $\gamma = 1.5$, $\gamma_L = 1.3$; (b) $\delta = 3.0$, $\gamma = 1.0$, $\gamma_L = 0.8$; (c) $\delta = 3.0$, $\gamma = 1.0$, $\gamma_L = 0.4$, $\eta = 2.0$.

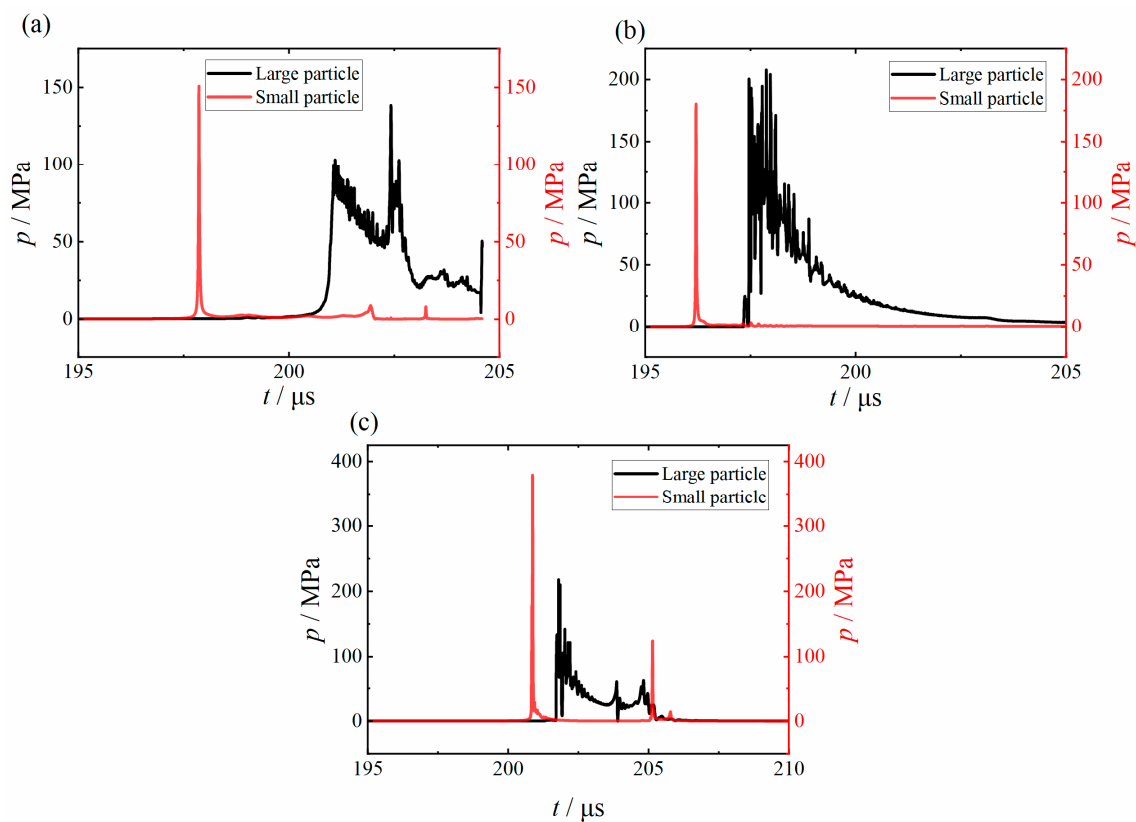


Figure 15. Temporal variation of surface pressure on the particles for case 3. The red curve depicts the pressure variations at the lower vertex of the small particle and the black curve depicts the pressure variations at the upper vertex of the large particle: (a) $\delta = 3.0$, $\gamma = 1.5$, $\gamma_L = 1.3$; (b) $\delta = 3.0$, $\gamma = 1.0$, $\gamma_L = 0.8$; (c) $\delta = 3.0$, $\gamma = 1.0$, $\gamma_L = 0.4$, $\eta = 2.0$.

In Figure 15a, since the jet carries the bubbles toward the large particle, the first pressure peak is induced by the jet impact, followed by a second peak from bubble collapse nearby. In Figure 15b, the direct impact of the jet on the large particle causes a sudden increase and then decrease in the surface pressure. In Figure 15c, for the large particle, after the jet impinges on it, the subsequent collapse of the bubbles leads to another increase in pressure. Meanwhile, for the small particle, the collapse and expansion of the nearby bubble (as observed in frames 4 and 5 of Figure 14c) result in another variation in its surface pressure.

6. Conclusions

The jet dynamics of a cavitation bubble collapsing between unequal-sized dual particles is investigated employing OpenFOAM solver. The accuracy of the solver is validated by comparing simulations with experimental data from a laser-induced bubble recorded by high-speed photography. The formation mechanism of jets is revealed through the pressure distribution and the velocity distribution of the liquid surrounding the bubble. The effects of the particle radius and bubble–particle distance on jet behavior and variations in particle surface pressure induced by the jet are explored. The following conclusions are drawn:

- (1) Our distinct jet behaviors are identified based on the formation mechanism, quantity, and direction of the jets. For case 1, a single jet toward the small particle. For case 2, double jets receding from each other. For case 3, double jets approaching each other. Case 4, a single jet toward the larger particle.
- (2) For the scenarios where the jet does not directly impact the particles, the increase in particle surface pressure is minimal.
- (3) When the bubble interface contracts to the symmetry axis, it induces a dramatic but short-duration variation in the particle surface pressure.

The present research delves into the dynamics of bubble jets near dual particles, thereby enhancing our comprehension of the underlying microscopic damage mechanisms of hydraulic–mechanical components operating in a sand-laden flow environment. Such knowledge is applicable to the design, production, operation, and maintenance of hydraulic machinery, aiding in ensuring its long-term safe and stable operation.

Author Contributions: Conceptualization, Z.W.; methodology, Z.W., Z.F. and J.H.; software, Z.F. and J.H.; validation, Z.F. and J.H.; formal analysis, Z.W. and Z.F.; investigation, Z.W., Y.Z. (Yuning Zhang 1) and Y.Z. (Yuning Zhang 2); resources, Y.Z. (Yuning Zhang 2); data curation, J.H.; writing—original draft, Z.W. and Z.F.; writing–reviewing and editing, Y.Z. (Yuning Zhang 1) and Y.Z. (Yuning Zhang 2); visualization, Z.F. and J.H.; supervision, Y.Z. (Yuning Zhang 1); project administration, Y.Z. (Yuning Zhang 1); funding acquisition, Y.Z. (Yuning Zhang 2). All authors have read and agreed to the published version of the manuscript.

Funding: This research was financially supported by the National Natural Science Foundation of China (Project No.: 52076215).

Data Availability Statement: The original contributions presented in the study are included in the article, further inquiries can be directed to the corresponding authors.

Conflicts of Interest: Author Zhifeng Wang was employed by the company State Power Investment Corporation. The remaining authors declare that the research was conducted in the absence of any commercial or financial relationships that could be construed as a potential conflict of interest.

Nomenclature

C_v	Specific heat capacity
d	Vertical distance from the origin to the bubble inception
D	Vertical separation between the upper vertex of the large particle and the lower vertex of the small particle
F_s	Surface tension
K	Fluid kinematic energy

K_l	Liquid constant of liquid phase
\dot{m}	Mass transfer rate
p	Fluid pressure
p_l	Pressure constant of liquid phase
R_L	Radius of large particle
R_{max}	Maximum radius of the bubble
R_S	Radius of small particle
R_v	Vapor constant
t	Time
T	Fluid temperature
T_l	Temperature constant of liquid phase
\mathbf{U}	Fluid velocity
\mathbf{U}_r	Relative velocity of the two phases

Greek letters

α	Volume fraction
ρ	Fluid density
μ	Fluid viscosity
ψ	Compressibility of fluid
τ	Viscous force tensor
λ	Thermal conductivity
δ	Dimensionless ratio of the radii between the large and the small particles
η	Dimensionless ratio of the radius of the large particle to R_{max} .
γ	Dimensionless distance between two particles
γ_L	Dimensionless distance between the location of bubble inception and the upper vertex of the large particle
γ_S	Dimensionless distance between the location of bubble inception and the lower vertex of the small particle

References

- Sun, J.; Ge, X.; Zhou, Y.; Liu, D.; Liu, J.; Li, G.; Zheng, Y. Research on synergistic erosion by cavitation and sediment: A review. *Ultrason. Sonochem.* **2023**, *95*, 106399. [[CrossRef](#)] [[PubMed](#)]
- Li, J.; Chen, X. A general two-phase mixture model for sediment-laden flow in open channel. *J. Hydrodyn.* **2022**, *34*, 286–298. [[CrossRef](#)]
- Zhang, W.; Zhu, B. Risk assessment of erosive aggressiveness due to the condensation shock by numerical simulation. *J. Hydrodyn.* **2022**, *34*, 200–206. [[CrossRef](#)]
- Sun, X.; Xia, G.; You, W.; Jia, X.; Manickam, S.; Tao, Y.; Zhao, S.; Yoon, J.Y.; Xuan, X. Effect of the arrangement of cavitation generation unit on the performance of an advanced rotational hydrodynamic cavitation reactor. *Ultrason. Sonochem.* **2023**, *99*, 106544. [[CrossRef](#)] [[PubMed](#)]
- Sergey, L.; Robert, M.; Gunther, B. Study of Ultrasound propagation and cavitation activity in a packing bed of spherical particles. *Chem. Ing. Tech.* **2017**, *89*, 1379–1384.
- Thomas, R.G.; Jonnalagadda, U.S.; Kwan, J.J. Biomedical applications for gas-stabilizing solid cavitation Agents. *Langmuir ACS J. Surf. Colloids* **2019**, *35*, 10106–10115. [[CrossRef](#)]
- Ren, L.Q.; Nitesh, N.; Jeffrey, M.M.; Fernandd, S.; Yan, Z.; Liu, W.; Wang, W.; Wang, J.; Thomas, E.M. 3D steerable, acoustically powered microswimmers for single-particle manipulation. *Sci. Adv.* **2019**, *5*, eaax3084. [[CrossRef](#)] [[PubMed](#)]
- Ladola, Y.S.; Chowdhury, S.; Roy, S.B.; Pandit, A.B. Application of cavitation in uranium leaching. *Desalination Water Treat.* **2014**, *52*, 407–414. [[CrossRef](#)]
- Filippov, L.O.; Royer, J.J.; Filippova, I.V. Improvement of ore recovery efficiency in a flotation column cell using ultra-sonic enhanced bubbles. *J. Phys. Conf. Ser.* **2017**, *879*, 012023. [[CrossRef](#)]
- Xu, W.; Zhang, Y.; Luo, J.; Zhang, Q.; Zhai, Y. The impact of particles on the collapse characteristics of cavitation bubbles. *Ocean. Eng.* **2017**, *131*, 15–24. [[CrossRef](#)]
- Chen, W.; Chen, X.; Zhang, J.; Wu, C.; Lu, Y.; Zhang, Z. The influence of coal particle shapes on the interaction behavior of air bubbles and coal particles. *Energy Sources Part A-Recovery Util. Environ. Eff.* **2022**, *44*, 3836–3849. [[CrossRef](#)]
- Lechner, C.; Lauterborn, W.; Koch, M.; Mettin, R. Fast, thin jets from bubbles expanding and collapsing in extreme vicinity to a solid boundary: A numerical study. *Phys. Rev. Fluids* **2019**, *4*, 021601. [[CrossRef](#)]
- Lechner, C.; Lauterborn, W.; Koch, M.; Mettin, R. Jet formation from bubbles near a solid boundary in a compressible liquid: Numerical study of distance dependence. *Phys. Rev. Fluids* **2020**, *5*, 093604. [[CrossRef](#)]
- Zevnik, J.; Dular, M. Cavitation bubble interaction with a rigid spherical particle on a microscale. *Ultrason. Sonochem.* **2020**, *69*, 105252. [[CrossRef](#)] [[PubMed](#)]

15. Dai, Y.; Zhang, H.; Chen, T. Influence of bubble-particle distance on the dynamic behaviors of a cavitation bubble near a particle. *J. Hydrodyn.* **2023**, *35*, 913–922. [[CrossRef](#)]
16. Lyu, F.; Zhang, X.; Yuan, H.; Han, S.; Tang, M. Research on the collapse characteristics of single cavitation bubble near solid particle by the VOF method. *Heliyon* **2023**, *9*, e21855. [[CrossRef](#)]
17. Li, S.; Han, R.; Zhang, A.M. Nonlinear interaction between a gas bubble and a suspended sphere. *J. Fluids Struct.* **2016**, *65*, 333–354. [[CrossRef](#)]
18. Chen, D.; Qiu, M.; Lin, Z.; Liu, Q.; Zhang, G.; Zhu, Z. Experimental study on the interaction of a cavitation bubble flanked by two particles. *Acta Mech.* **2021**, *232*, 4801–4810.
19. Hu, J.; Lu, X.; Liu, Y.; Duan, J.; Liu, Y.; Yu, J.; Zheng, X.; Zhang, Y.; Zhang, Y. Numerical and experimental investigations on the jet and shock wave dynamics during the cavitation bubble collapsing near spherical particles based on OpenFOAM. *Ultrason. Sonochem.* **2023**, *99*, 106576. [[CrossRef](#)]
20. Wang, X.; Zhang, C.; Su, H.; Li, S.; Shen, J.; Zhang, Y.; Li, J. Research on cavitation bubble behaviors between a dual-particle pair. *Phys. Fluids* **2024**, *36*, 3310. [[CrossRef](#)]
21. Chen, S.; Xu, W.; Luo, J.; Li, J.; Zhai, Y. Experimental study on the mesoscale causes of the effect of sediment size and concentration on material cavitation erosion in sandy water. *Wear* **2022**, *488*, 204114. [[CrossRef](#)]
22. Greenshields, C. *OpenFOAM v11 User Guide*, 1st ed; The OpenFOAM Foundation: London, UK, 2023; p. 422.
23. Tian, L.; Zhang, Y.; Yin, J.; Lv, L.; Zhang, J.; Zhu, J. Study on the liquid jet and shock wave produced by a near-wall cavitation bubble containing a small amount of non-condensable gas. *Int. Commun. Heat Mass Transf.* **2023**, *145*, 106815. [[CrossRef](#)]
24. Xia, G.; You, W.; Manickam, S.; Yoon, J.Y.; Xuan, X.; Sun, X. Numerical simulation of cavitation-vortex interaction mechanism in an advanced rotational hydrodynamic cavitation reactor. *Ultrason. Sonochem.* **2024**, *105*, 106849. [[CrossRef](#)] [[PubMed](#)]
25. Li, W.; Yu, X. Cavitation models with thermodynamic effect for organic fluid cavitating flows in organic Rankine cycle systems: A review. *Therm. Sci. Eng. Prog.* **2021**, *26*, 101079. [[CrossRef](#)]
26. Deshpande, S.S.; Anumolu, L.; Trujillo, M.F. Evaluating the performance of the two-phase flow solver interFoam. *Comput. Sci. Discov.* **2012**, *5*, 014016. [[CrossRef](#)]
27. Shin, B.R.; Iwata, T.; Ikohagi, T. Numerical simulation of unsteady cavitating flows using a homogenous equilibrium model. *Comput. Mech.* **2003**, *30*, 388–395. [[CrossRef](#)]

Disclaimer/Publisher's Note: The statements, opinions and data contained in all publications are solely those of the individual author(s) and contributor(s) and not of MDPI and/or the editor(s). MDPI and/or the editor(s) disclaim responsibility for any injury to people or property resulting from any ideas, methods, instructions or products referred to in the content.